J. Fluid Mech. (2006), *vol.* 561, *pp.* 439–463.
doi:10.1017/S0022112006000954 Printed in the United Kingdom

Shear flow past two-dimensional droplets pinned or moving on an adhering channel wall at moderate Reynolds numbers: a numerical study

By PETER D. M. SPELT

Department of Chemical Engineering, Imperial College London, SW7 2AZ, UK

(Received 4 August 2005 and in revised form 25 January 2006)

Numerical simulations are presented of shear flow past two-dimensional droplets adhering to a wall, at moderate Reynolds numbers. The results were obtained using a level-set method to track the interface, with measures to eliminate any errors in the conservation of mass of droplets. First, the case of droplets whose contact lines are pinned is considered. Data are presented for the critical value of the dimensionless shear rate (Weber number, We), beyond which no steady state is found, as a function of Reynolds number, Re. We and Re are based on the initial height of the droplet and shear rate; the range of Reynolds numbers simulated is $Re \leqslant 25$. It is shown that, as Re is increased, the critical value We_c changes from $We_c \propto Re$ to $We_c \approx$ const., and that the deformation of droplets at We just above We_c changes fundamentally from a gradual to a sudden dislodgement. In the second part of the paper, drops are considered whose contact lines are allowed to move. The contact-line singularity is removed by using a Navier-slip boundary condition. It is shown that macroscale contact angles can be defined that are primarily functions of the capillary number based on the contact-line speed, instead of the value of We of the shear flow. It is shown that a Cox–Voinov-type expression can be used to describe the motion of the downstream contact line. A qualitatively different relation is tested for the motion of the upstream contact line. In a third part of this paper, results are presented for droplets moving on a wall with position-dependent sliplength or contact-angle hysteresis window, in an effort to stabilize or destabilize the drop.

1. Introduction

Shear flow past droplets or bubbles adhering to a solid surface is relevant in a range of applications. These include oil or grease removal in detergency (Chatterjee 2001), the entrainment of leukaemic cells from a blood vessel wall by blood flow (Cao *et al.* 1998), bubble detachment from a heated pipe wall in boilers (Hewitt 1978; Duhar & Colin 2004), and, for the curious train passenger, the motion of rain drops on window panes (Minnaert 1974). A study in shear flow past droplets adhering to a wall also provides a first step towards understanding membrane emulsification. In such emulsification processes, liquid is pumped through a membrane into a crossflow of another liquid, which shears off droplets to form an emulsion (see Charcosset, Limayern & Fessi 2004).

Previous work on this problem has been primarily on creeping flows past pinned drops and bubbles. Wakiya (1975) provides an analytical solution of shear flow past

a solid cylinder on a wall, elucidating the occurrence of Moffatt eddies in corners. This may serve in the present context as a limiting case, for highly viscous drops. Li & Pozrikidis (1996), Yon & Pozrikidis (1999) and Dimitrakopoulos & Higdon (1997, 1998, 1999, 2001) studied in detail the steady-state creeping flow past a droplet or bubble whose contact line is pinned. These studies focused primarily on the determination of critical values of parameters for given values of the contact angles, beyond which no steady state can be found. The relevant parameters for creeping flows are a capillary number, the window of contact angles within which the contact line does not move owing to hysteresis (Dussan V. 1979), and the viscosity ratio of the two fluids.

Present understanding of these flows is therefore limited to steady-state creeping flows past pinned droplets, with some exceptions discussed below. In this paper, the effects of inertia will be studied. In order to provide the strong basis needed to understand the corresponding three-dimensional flows, we study here in detail the two-dimensional problem. One of the main features in creeping flow past three-dimensional pinned droplets is that the drops exhibit strong fore-and-aft asymmetry. The contact angle on either side is approximately constant, as shown by Dimitrakopoulos & Higdon (1998). Therefore, a study of the two-dimensional problem is expected to reveal the most significant inertial effects on (for example) the stability of droplets. Some of the trends observed for the three-dimensional creeping-flow problem (e.g. the role of the viscosity ratio) were explained by Dimitrakopoulos & Higdon (1998) using arguments similar to those in their study of the two-dimensional problem. Furthermore, as explained in some detail by Dimitrakopoulos & Higdon (1999), it is expected that droplets can be made to spread in the cross-flow direction (such that the two-dimensional system is approached) by choosing the appropriate initial configuration. Such droplets are more stable than others, as an increased width of the droplet would result in a larger resistance to the interfacial stresses acting on the drop. A secondary motivation for the present two-dimensional study is that, even for the two-dimensional creeping-flow problem, the velocity of the contact lines has not yet been related to a macroscopic contact angle, with the exception of work by Hodges & Jensen (2002). The latter authors used lubrication theory to determine the relation between contact-line speed, macroscopic contact angles and the applied shear rate for a two-dimensional cell rolling over a substrate.

A first aim of the present paper is to investigate the role of inertia, in particular, on the conditions beyond which no steady state is observed. Feng & Basaran (1994) studied steady-state shear flow with inertia past a pinned (two-dimensional) bubble, showing that the critical shear rate beyond which no steady solution is found and flow fields are determined primarily by a Weber number, the results being not sensitive to the Reynolds number. It is difficult to generalize results for bubbles to droplets, however. The deformation of a bubble is due to normal stresses, because of the zero tangential stress at the interface, whereas droplet deformation results from tangential stress components as well. Dimitrakopoulos & Higdon (1997) used lubrication theory to show that the yield criteria are very different for thin drops and bubbles. A study of shear flow with inertia past a pinned droplet will be presented in § 3. It is valuable in some applications to know how droplets deform if no steady solution exists (e.g. in emulsification). Therefore, § 3 also includes results for cases in which no steady state occurs.

In the second part of this paper, cases are studied in which droplets start to slide along the wall. Whether a simple approximate description can be obtained of the motion of the contact lines will be investigated. Early work on this problem was reported

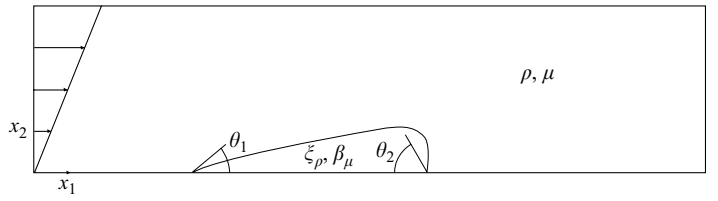

FIGURE 1. Sketch of the problem. Spatial coordinates and lengths are made dimensionless with the channel height, velocity components by the velocity of the upper wall.

by Dussan V. (1987), who used lubrication theory to derive a yield criterion for flat three-dimensional droplets. Following the work cited above on pinned drops that are not thin, Schleizer & Bonnecaze (1999) presented boundary element simulations for two-dimensional droplets in which the contact lines were allowed to move. Those authors used a constant contact angle in their simulations of sliding drops. They conducted some preliminary experiments, which appeared to show that the contact angle did not change significantly during the sliding motion. In order to alleviate the stress singularity at moving contact lines (Huh & Scriven 1971), Schleizer & Bonnecaze (1999) used an approximate integrated form of the Navier slip condition (see also figure 1)

$$u_1 = \lambda \frac{\partial u_1}{\partial x_2}, \tag{1.1}$$

where u_1 is the dimensionless fluid velocity component along the wall, x_2 is the dimensionless coordinate normal to the wall, and λ is the dimensionless sliplength. Throughout this paper, spatial coordinates and other length scales have been made dimensionless with the height of the channel, and velocity components with the velocity of the upper channel wall shown in figure 1). Simulating flows for a small value of λ requires excessive computational efforts. Schleizer & Bonnecaze (1999) presented results for a fixed (inferred) slip length, of $\lambda \approx 0.005$. (In the present notation, the dimensionless channel height is unity, which introduces a factor of 2 when comparing results with theirs, also in the capillary number.) They showed that allowing the contact line to move leads to a significant reduction in the critical values of dimensionless parameters for creeping flows. They argued that this is a consequence of the reduced relative velocity between the two fluids, the time-independence of the contact angles, and an observed reduction in height at relatively low contact angle values. However, no relation between a macroscopic and microscopic contact angle was proposed by these authors.

In the simulations of flows with moving contact lines reported here, the slip condition (1.1) is implemented directly; and this allows us to assess directly the effect of surface properties. Also, inertial effects are accounted for. There are several other ways of eliminating the stress singularity. These include: (*a*) assuming a diffuse instead of a sharp interface (resulting in a flux through the interface near the contact line, representing site changes between the two fluids (Jacqmin 2000; Briant & Yeomans 2004)); (*b*) condensation or evaporation (Briant, Wagner & Yeomans 2004) (when appropriate); (*c*) the introduction of a precursor layer (such that the entire wall is wetted, e.g. de Gennes 1985); and (*d*) accounting for surface tension relaxation (Shikhmurzaev 1997). A slip condition is a pragmatic way to alleviate the stress singularity for non-smooth walls, which are relevant in practical applications. There appears to be little rigorous justification for clean smooth walls, however. A thermodynamic justification for a diffuse interface (which does not require slip) is available,

but the underlying assumption that interfaces are sufficiently thick so that composition gradients through them can be differentiated, is highly questionable (Jacqmin 2000). Nevertheless, evidence indicates that both schemes give virtually identical quantitative results for the flow outside the very small contact-line region (Jacqmin 2004). A slip condition is still widely used (e.g. Hocking & Davis 2002).

In order to account for inertial effects whilst attempting to simulate moving contact lines accurately, a numerical technique recently developed by the author (Spelt 2005) is used here. This is a level-set approach for the simulation of flows at moderate Reynolds numbers with moving contact lines. Evidence of convergence, and a comparison with well-established relations for spreading droplets have been published in the previous work (Spelt 2005). The problem formulation and a summary of the numerical method are given in § 2. Evidence that the present method conserves the mass of an entire droplet is presented in the Appendix.

In § 4, the range of simulations presented by Schleizer & Bonnecaze (1999) for moving drops in creeping flow is extended by including inertial effects. Following Schleizer & Bonnecaze (1999), the contact angles are kept constant in the simulations. Since the contact-line speed decreases when λ is decreased, a specific point of interest is the sensitivity of yield criteria to the sliplength. It is shown that, as in droplet spreading, macroscale angles can be defined that are functions of the instantaneous value of $Ca^{cl} = \mu U^{cl}/\sigma$ only (for a given contact angle, and the viscosity and density ratios set to unity), as in Cox–Voinov-type relations (Cox 1986). Here, μ is the fluid viscosity, σ the coefficient of surface tension, and U^{cl} is the contact-line speed. These macroscale contact angles appear to be independent of Re and We for the cases simulated. For example, for the downstream contact line, it is shown that we can write

$$\theta_m = F(Ca^{cl}, \theta_2, \lambda, \beta, \xi), \tag{1.2}$$

where θ_m is the maximum angle between the interface (in the neighbourhood of the contact line) and the x_1-axis; β and ξ are the viscosity and density ratio (see figure 1). For the upstream contact line, although a different macroscale angle must be used, a similar relation is obtained. Since the value of λ in practical applications is extremely small (well beyond the capabilities of most numerical methods), such relations can be used to simulate the macroscale only (Spelt 2005). This is discussed further in the § 6.

The final part of this paper investigates the sensitivity of the results to the surface properties, and examines whether crawling drops can be stabilized or destabilized by exposing them to a locally altered surface. This problem is also of interest for applications in which the wall does not have perfectly homogeneous wetting properties. In these simulations, either the sliplength is different in two parts of the wall or the window of contact-angle hysteresis. The resulting unsteady behaviour is also considered as a test for relations such as (1.2).

2. Formulation and method

2.1. *Problem formulation*

The flow sketched in figure 1 starts from rest at time $t = 0$, when the upper plate is set in motion impulsively. Spatial variables are made dimensionless with the channel height, velocities with the velocity of the top wall V, and time with the ratio of channel height H and top wall velocity. The flow is governed by the Navier–Stokes equations, subject to the following boundary conditions: at the entrance, the unidirectional start-up shear flow is imposed (Leal 1992, p. 102); at the exit, $\partial u_1/\partial x_1 = 0$ and $u_2 = 0$,

where u_j denotes the velocity component in the x_j-direction (see figure 1). At the top wall, $(u_1, u_2) = (1, 0)$. The boundary condition at $x_2 = 0$ is also a no-slip for pinned drops and bubbles; for moving contact lines, $u_2(x_2 = 0) = 0$ and (1.1) at $x_2 = 0$, such that the stress singularity at moving contact lines is alleviated. We note here that (1.1) is imposed along the entire wall. If λ is taken to be sufficiently small, slip will only be significant in regions of large wall shear stress (i.e. the moving contact lines).

The slip condition (1.1) must be supplemented by a contact-line law (Davis 2000). We use here the approximate law

$$\left.\begin{array}{lll} \theta_i = \theta_A & \text{if} & U_i^{cl} > 0, \\ \theta_i = \theta_R & \text{if} & U_i^{cl} < 0, \\ \theta_R \leqslant \theta_i \leqslant \theta_A & \text{if} & U_i^{cl} = 0, \end{array}\right\} \tag{2.1}$$

where θ_i, θ_A and θ_R are the dynamic, advancing and receding contact angle, respectively, $i = (1, 2)$ and U_i^{cl} is the contact-line velocity of contact line i (which is positive here for a spreading droplet). Typical experimentally observed trends in relations between contact angle and contact-line speed are discussed by Dussan V. (1979).

2.2. *Dimensionless parameters*

The following independent dimensionless numbers will be used, adopting the notation of figure 1. The Reynolds and Weber numbers of the external fluid are $Re = \rho a^2 \gamma / \mu$ and $We = \rho a^3 \gamma^2 / \sigma$, where $\gamma = V/H$ is the shear rate and a is the initial drop radius. The capillary number is $Ca = \mu a \gamma / \sigma = We/Re$. The viscosity and density ratio are denoted by β and ξ, respectively; the dimensional values $\theta_{A,R}$ will be used. Unless indicated otherwise, $\xi = 1$. To keep the number of dimensionless parameters manageable, gravitational effects are not taken into account in this paper. The initial shape of the droplet is circular. The geometry of the problem involves the aspect ratio of the channel, the initial contact angle values, the dimensionless cross-sectional area of the drop or bubble (denoted by A), and the distance between the entrance and the droplet centre. In most calculations for pinned drops, the channel aspect ratio is 4, unless indicated otherwise. The distance between the droplet centre to the entrance is 1.4 and 0.7 in these cases, respectively.

2.3. *Numerical method and comparison with previous work*

The level-set approach of Spelt (2005) is used here, as an extension of the single-grid two-dimensional version of the method of Sussman *et al.* (1999), to account for moving contact lines. A finite-difference method is used, with a partially staggered grid: velocity components are defined at cell centres, the pressure at cell vertices. The equations of motion for each fluid are combined into one set of continuity and momentum equations, with variable density and viscosity and a momentum source term due to surface tension. These equations are solved numerically using a projection method. The interface is tracked through the so-called level-set function $\phi(\boldsymbol{x}, t)$, which is defined as a signed distance function (at cell centres), such that $|\phi(\boldsymbol{x}, t)|$ is the distance of $\boldsymbol{x}$ at time t from the nearest interface. The sign is different on either side of the interface, and the interface location corresponds to $\phi = 0$. Because the interface is advected by the fluid, ϕ is determined from the solution of an advection equation. The advection equation only holds at $\phi = 0$, however, and, after each time step a 'redistance' step is performed, to ensure that ϕ at points away from the interface is again approximately the signed distance function. The local density and viscosity values follow directly from ϕ, as does the curvature (which occurs in the momentum source term arising from surface tension forces). Details of the method have been

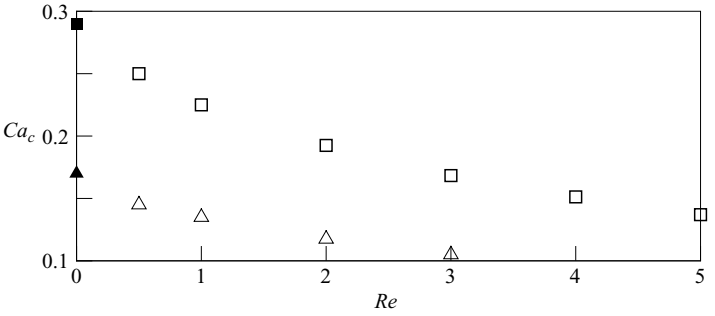

FIGURE 2. Comparison with creeping-flow results of Schleizer & Bonnecaze (1999) (filled symbols) for critical capillary number. Open symbols represent present results. □, $\beta = 1$, $A = 0.03125$; △, $\beta = 8$, $A = 0.125$.

published by Sussman *et al.* (1999). The derivation of the stress term and the related momentum source due to surface tension has been presented by Chang *et al.* (1996).

Tests showed that the method of Sussman *et al.* (1999) results in a significant drop size reduction during simulations. In the Appendix, we verify that a recent modification of the redistance step algorithm (Russo & Smereka 2000; Spelt 2005) eliminates this problem for a case representative for the fluid flows considered in this paper, without affecting the dynamics of the simulations significantly.

The position of contact lines for pinned drops, and the contact-line law (2.1) for moving drops are enforced by prescribing the value of ϕ at ghostcells. The contact lines could be pinned throughout a simulation by prescribing zero contact-line speed, with $\theta_R = 0$ and $\theta_A = 180^\circ$. The numerical procedure for the prescription of ϕ at ghostcells is given in detail in Spelt (2005).

Results of various test cases using the code were presented by Spelt (2005), including a comparison against lubrication theory for spreading of flat droplets. The lubrication theory results in a matching condition, which relates a macroscopic contact angle to the microscopic contact angle. The macroscopic angle was approximated by the maximum value of the angle that the interface makes with the horizontal. This angle was plotted as a function of the capillary number based on the contact-line speed. It was shown that the result approaches that of the lubrication theory at low-capillary-number values, as the numerical grid is refined. A reasonably accurate result was obtained when the grid spacing is approximately equal to the slip length. It is also clear from the results presented by Spelt (2005) that a coarser mesh leads to an overprediction of the contact-line speed. This is consistent with the notion that discretization errors lead to some numerical slip. At several key points in § 4, results are shown for two different values of the grid spacing.

Results were also compared with those of Schleizer & Bonnecaze (1999) for the present problem in the creeping-flow limit (a comparison was made of the steady-state shape of the drops). To supplement these data, we compare in figure 2 the critical value of Ca beyond which no steady state is found with the corresponding result of Schleizer & Bonnecaze (1999), for pinned drops. As Re is decreased, the BEM results for $Re \to 0$ are approached. The equations of motion become very stiff in the limit $Re \to 0$, explaining the absence of results for very low values of Re in this figure. At the lowest values of Re simulated, it was found that a steady state can be reached even for a very strongly deformed droplet. Although large deformations can be simulated with the present method, such a steady state is achieved only after a

very long integration time, and a minimum value of $Re = 0.5$ was typically used in the simulations reported here.

In this work, the jump in viscosity across the interface is treated numerically as in Chang *et al.* (1996) and Sussman *et al.* (1999): the local viscosity value is $\mu(H(\phi)+\beta(1-H(\phi))$, where $H(\phi)$ is a smoothed step function. The smoothing of the step function occurs over a distance that is proportional to the grid spacing, such that the real step function is approached when a fine numerical grid is used. The work of Magnaudet, Bonometti & Benkenida (2006) indicates that the use of such conventional smoothing of the viscosity jump across the interface may lead to significant errors for simulations of flows at very small or large values of β. We can infer from the results in figure 2 for $\beta = 8$ that the range of values of β studied here ($0.1 \leqslant \beta \leqslant 10$) is tolerable. An accurate comparison with the simulations of Feng & Basaran (1994) would have been desirable, because it would test the accuracy of the predicted inertial effects. However, this would require an approach to the limit $\beta = 0$ (and $\xi = 0$), as well as a very small value of A, and has therefore not been pursued. The density is obtained from the level-set function, such that $\mathrm{D}\rho/\mathrm{D}t = (\mathrm{d}\rho/\mathrm{d}\phi)\mathrm{D}\phi/\mathrm{D}t$. If no redistance step is performed in the level-set method, $\mathrm{D}\phi/\mathrm{D}t = 0$. The redistance step results in $\mathrm{D}\phi/\mathrm{D}t \neq 0$ for points away from the interface (at the interface itself, the redistance step has no effect). This will result in finite compressibility, but only in the narrow region around the interface (1.5 times the grid spacing on either side of the interface). Any effect of compressibility should vanish as the grid spacing is decreased. Results of different mesh sizes will be shown to indicate the magnitude of discretization errors involved.

The numerical method was used to integrate the equations of motion starting from rest. A square mesh is used, and the channel height was divided into 2^N grid cells. Where applicable, the value of N used in the simulations is stated in the figure captions. The upper wall was set in motion impulsively at $t = 0$ (figure 1). The critical value of We_c (or Ca_c) was obtained by increasing We until no steady solution was found. A case was declared steady when the drop perimeter had changed less than 1% over a time interval of $0.2T$, but such that at least $t = T$ had elapsed, where $T = \max\{H^2\rho/\mu, H^2\rho\xi/(\beta\mu)\}$. If a case was found not to be steady after $t = 2T$ it was declared unsteady. In certain cases (especially those for large β shown in figure 2), a larger integration time was required.

3. Results for pinned contact lines

A typical flow pattern for a pinned-contact-line case in which a steady state is reached is shown in figure 3 for $Re = 10$. This is for viscosity- and density-matched fluids. A stationary wake has been formed in this case. Because the fluid in the wake rotates in the same sense as the vortex initiated inside the drop, it is separated from the droplet. A streamline very close to the drop surface is seen to make a U-turn between drop and wake. The wake is very weak (the streamfunction is less than 10^{-4} for the case shown), and was found to be absent for relatively large drops as well as for low values of Re. It should be noted that the streamfunction shown in figure 3 was obtained from the velocity field by solving $\nabla^2\psi = -\omega$, by using a finite-difference approximation for the Laplacian and the vorticity ω. Therefore, errors in the streamfunction contours of figure 3 are not necessarily representative of those of the velocity field.

Figure 2 shows the significance of inertial effects for pinned contact lines. Ca_c decreases rapidly when Re is increased, and Re will have to be significantly less than

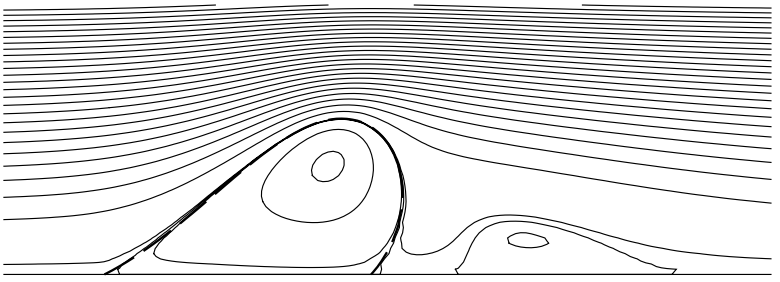

FIGURE 3. Streamfunction contours just below We_c for $\beta = 1$, $A = 0.25$, $Re = 10$, $We = 0.58$, $N = 6$ (detail). Initial contact angles are 90°. The streamfunction ψ was obtained from the velocity field using a finite-difference approximation for the vorticity. The spacing between contours corresponds to a difference in streamfunction value of 0.0125; $\psi = \pm 4 \times 10^{-4}$ are also shown. The dashed line (which is virtually unobservable as it coincides with $\psi = 0$) corresponds to the drop surface, $\phi = 0$. A wake is not observed for $A = 0.5$ at $Re = 10$.

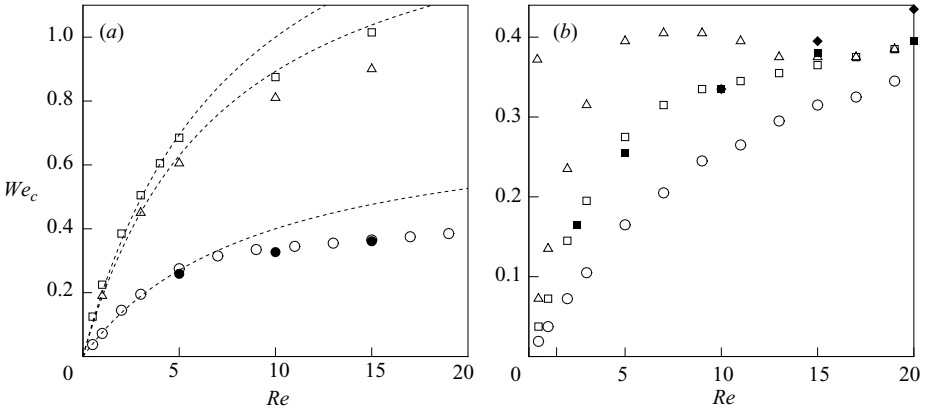

FIGURE 4. Critical Weber number as a function of Reynolds number, showing the effect of channel dimensions (a), viscosity ratio β and density ratio ξ (b). (a) $\xi = 1$; $\beta = 1$, (□); $A = 0.03125$, $N = 6$, (Δ); $A = 0.125$, $N = 5$; (○); $A = 0.5$, $N = 5$ (open symbols) and $N = 6$ (filled symbols). The dashed lines represent (3.2), using a curve fit for the parameters, as indicated in the main text. (b) $A = 0.5$, $\xi = 1$ (open symbols), $\xi = 10$ (filled symbols), $N = 5$ unless indicated otherwise. □, $\beta = 1$; Δ, $\beta = 0.1$; ○, $\beta = 10$. The filled diamonds are for $N = 6$, $\xi = 10$, $\beta = 1$ ($Re \geqslant 10$ only). Contact angles at $t = 0$ are 90° in all cases.

unity for $Ca_c(Re)$ to be approximated well by $Ca_c(Re = 0)$. At values of Re significantly above unity, it is anticipated that the critical shear rate is a constant. Noting that $Ca_c = We_c/Re$, the expectation is therefore that Ca_c decreases when Re is increased. In figure 4(a), We_c is plotted against Re for different values of A. Qualitatively, the same trend is seen for any value of A. A transition occurs from the creeping-flow limit (in which $We_c \sim Re$) to a moderate-Re regime in which We_c is independent of Re. The latter regime has been identified previously by Feng & Basaran (1994) for pinned bubbles.

In figure 4(b), results are presented for different values of the viscosity ratio β and density ratio ξ. Since the density ratio drops out of the analysis for creeping flows, We would be expected to be independent of ξ at low Re. In fact, the dependence on ξ is seen to be minimal at all values of Re simulated. Also, at sufficiently large Re, We_c appears to be virtually independent of β. At relatively low values of Re, the slope of

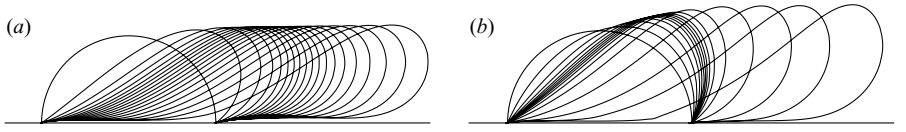

FIGURE 5. Different transient behaviour at low and moderate Re. Interface shapes are shown at constant time intervals for $We > We_c$: (*a*) $Re = 5$, $We = 0.262$; (*b*) $Re = 15$, $We = 0.362$. The time interval between successive frames is $0.4H^2\rho/\mu$ and $0.16H^2\rho/\mu$, respectively; $\beta = 1$, $A = 0.5$, $N = 6$. The droplets rupture in the simulations at a time just after the final shape shown.

We_c (i.e. Ca_c) decreases significantly when λ is increased. This is consistent with the findings of Dimitrakopoulos & Higdon (1997) for creeping flows (note, however, that they also showed that Ca_c is independent of β for thin drops), and Schleizer & Bonnecaze (1999). The total drag on droplets is due to normal and tangential stresses. For bubbles ($\beta = 0$, $\xi = 0$), the tangential stress component vanishes at the interface, so it is expected that more viscous drops experience a larger drag owing to the additional tangential stresses. This can be quantified for the case that $Ca \ll 1$, $A \ll 1$ and the contact angles are 90°. Integration of the analytical solution derived by Feng & Basaran (1994) shows that the drag force on such a bubble is $4\mu\gamma a$. The corresponding drag on a solid no-slip cylindrical projection is $4\mu\gamma a/(1 - 4/\pi^2)$ (Wakiya 1975). The drag force is therefore written as $\alpha_v\mu\gamma a$, where α_v is expected to vary gradually between these limiting values.

Dimitrakopoulos & Higdon (1997) used a force balance to estimate Ca_c for creeping flows past a pinned slender drop. We shall describe here the dependence of We_c on Re using similar arguments for flows with inertia. As a simple scaling argument, the drag force per unit width of the drop consists of a viscous component ($\alpha_v\mu a\gamma$), resulting from tangential and normal stresses, and a form drag, which is tentatively written as $\alpha_F\rho a^2\gamma^2$. At steady state, this drag, together with the integrated wall shear stress (written here as $\alpha_w\mu a\gamma$), are balanced by the force applied at the contact line ($\sim \sigma(\cos\theta_1 - \cos\theta_2)$). This results in

$$\cos\theta_1 - \cos\theta_2 \approx (\alpha_v + \alpha_w)We/Re + \alpha_F We. \tag{3.1}$$

Tests indicated that the wall stress contributes only a fraction to the total drag force.

Assuming for the time being that all constants are only weak functions of We and Re, and that at all values of Re, $We = We_c$ coincides with the point at which $\theta_1 = 0$, $\theta_2 = 180°$ (this is tested below), it follows that

$$We_c \approx 2\,((\alpha_v + \alpha_w)/Re + \alpha_F)^{-1}. \tag{3.2}$$

This approximation is compared with numerical simulations in figure 4(*a*). Since $\alpha_v + \alpha_w$ and α_F are unknown, these were obtained from a curve-fit, and the comparison can only be qualitative. The fitted values are: $(\alpha_v + \alpha_w, \alpha_F) = (24, 2.6)$, $(9.4, 1.3)$ and $(8.8, 1.1)$ for $A = 0.5$, 0.125 and 0.03125, respectively. (The value for $\alpha_v + \alpha_w$ does compare reasonably well with the expected range of values for α_v cited above.) It is seen that (3.2) can represent the data well for values of $Re \leqslant 5$; but if the same values of the fitted coefficients are used at larger Re, We_c is overpredicted. We shall discuss this discrepancy again later in this section. Despite the discrepancy at higher Re, (3.2) serves to capture the first deviation from the creeping-flow results for We_c, if Re is increased from zero. Also, to complete the case made above that α_v is an increasing function of β, we would expect from (3.2) that We_c decreases with increasing β at low Re, in agreement with figure 4(*b*).

It was observed that the flow conditions at the onset of entrainment are fundamentally different at low and moderate values of Re. In figure 5, snapshots

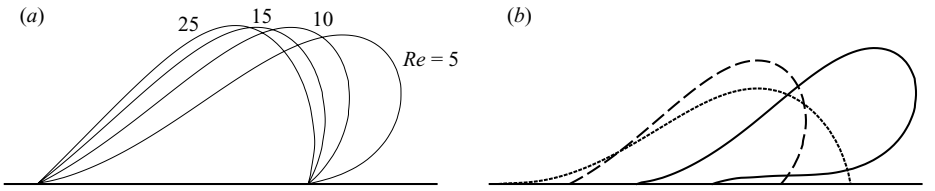

FIGURE 6. Steady-state droplet shape for We just below We_c at $\beta = 1$, for various values of Re (a) and the initial contact angles (b). (a) (Re, We) = (5, 0.254), (10, 0.328), (15, 0.36) and (25, 0.39); initial contact angles, 90°; $A = 0.5$. (b) Initial contact angles of 45° (short dashes), 90° (long dashes) and 150° (solid line). $Re = 10$ and $We = 0.3$, 0.58, 0.9, respectively. $A = 0.25$, $N = 6$.

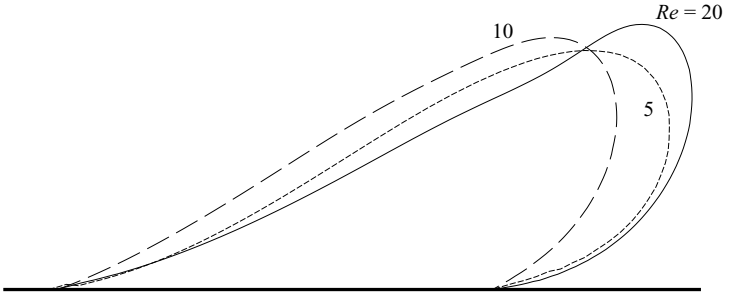

FIGURE 7. Steady-state droplet shape for We just below We_c at $\beta = 10$, for various values of Re as indicated. Initial contact angles are 90°; $N = 6$ ($Re = 10$ and 20), $N = 5$ ($Re = 5$), $A = 0.5$. (Re, We) = (5, 0.25), (10, 0.33) and (20, 0.41).

of the drop shape are shown for successive time intervals at We just above its critical value, for $Re = 5$ and $Re = 15$. At $Re = 5$, the droplet is seen to deform gradually in this figure, with θ_1 and θ_2 approaching 0° and 180°, respectively. At $Re = 15$, the drop appears to approach a steady state but, as the fluid continues to accelerate, the droplet is suddenly deformed drastically.

A fundamental difference in conditions at the onset of instability was also shown by Feng & Basaran (1994) for pinned bubbles: at low Re, bubbles are extended along the direction of principal extension (the so-called 'skewing mode'), whereas at large Re, bubbles are stretched upward (the 'erecting mode'). As pointed out by Dimitrakopoulos & Higdon (1997), however, it is difficult to extrapolate results of bubbles to drops, owing to the absence of shear stress on the interface in the former.

The droplet interface at We just below We_c is presented for several values of Re (with $\theta_1(t = 0) = \theta_2(t = 0) = 90°$, $\beta = \xi = 1$) in figure 6(a). It is seen that the droplet hardly deforms at all for $We < We_c$ at $Re = 25$, in sharp contrast to the low-Re shape. Unlike the 'erecting mode' of Feng & Basaran (1994), the interface on the upstream side is virtually straight, and no clear upper tip develops in the interface. In figure 6(b), it is seen that an initially slender droplet at these moderate values of Re will tend to become unstable because θ_1 approaches zero. A droplet with large initial contact angles results in a large value of θ_2, close to $\phi = 180°$ at the onset of instability.

In figure 7, it can be seen that some of these trends carry over to droplets with a density larger than that of the surrounding fluid ($\xi = 10$). As Re is increased from 5 to 10, the droplet is seen to be less deformed at the onset of instability. At the largest value of Re simulated ($Re = 20$), however, the droplet is deformed strongly at the onset of instability. (The slow rate of convergence of the numerical results in

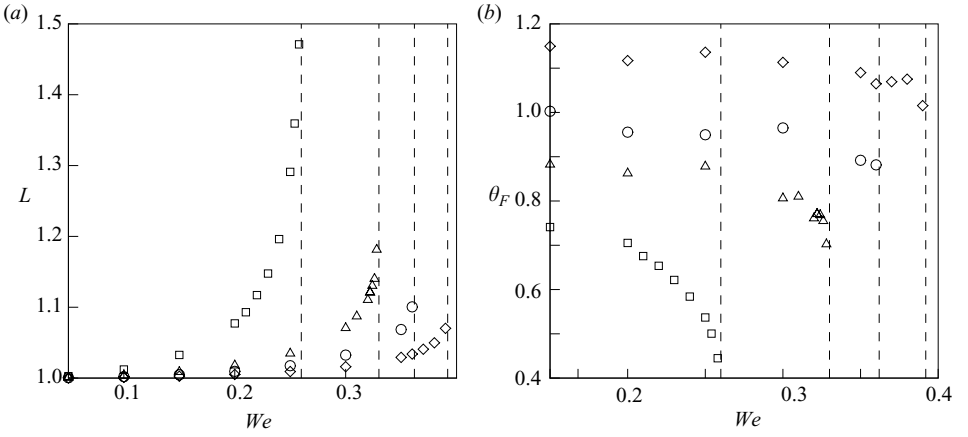

FIGURE 8. Surface length L (a) and angle of maximum deformation θ_F (b) for $A=0.5$, $\beta=1$ at fixed Reynolds number, as a function of *We*. □, $Re=5$; Δ, $Re=10$, ○, $Re=15$, ◇, $Re=25$. $N=6$. The dashed lines indicate the lowest value of *We* for which no steady state was found for each case. Contact angles at $t=0$ are 90° in all cases.

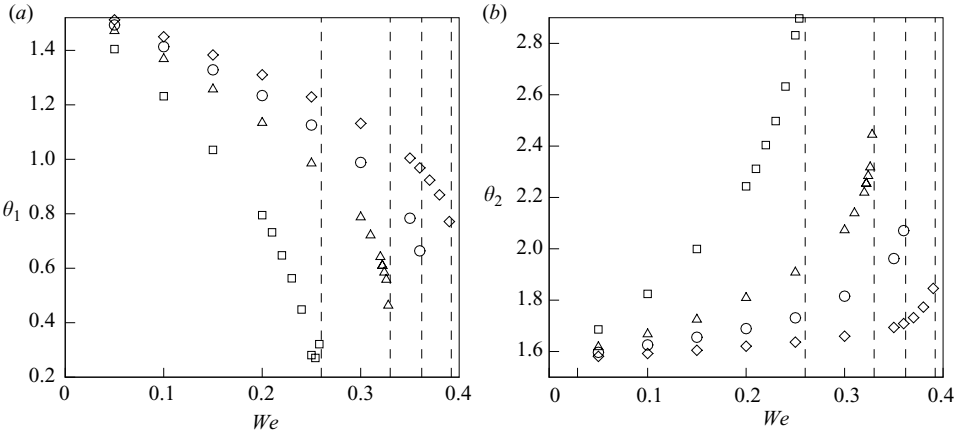

FIGURE 9. Steady-state contact angles (a) θ_1 and (b) θ_2 for $A=0.5$, $\beta=1$ at fixed Reynolds number, as a function of *We*. □, $Re=5$; Δ, $Re=10$; ○, $Re=15$; ◇, $Re=25$. $N=6$. The dashed lines indicate the lowest value of *We* for which no steady state was found for each case. Contact angles at $t=0$ are 90° in all cases.

this case (see figure 4b) can possibly be attributed to the approach of θ_1 to zero, and θ_2 to 180°.) Inspection of the results has shown that the vortical structure inside the drop (see figure 3) is only present in the upper part of the drop when $\xi=10$, with the lower part being almost stationary; this is not observed when $\xi=1$. These different regions inside the drop explain the peculiar wobbly shape of the upstream part of the interface seen in figure 7.

Quantitative information on these trends for $\beta=\xi=1$, $\theta_1(t=0)=\theta_2(t=0)=90°$ is presented in figures 8 and 9. In figure 8(a), the ratio of the droplet perimeter at steady state with its value at $t=0$ is plotted against *We*, for various values of *Re*. The vertical dashed lines indicate the lowest value of *We* at which no steady state was found. Whereas the perimeter ratio L appears to increase almost indefinitely as $We \to We_c$ at low *Re*, this is not so at $Re > 10$.

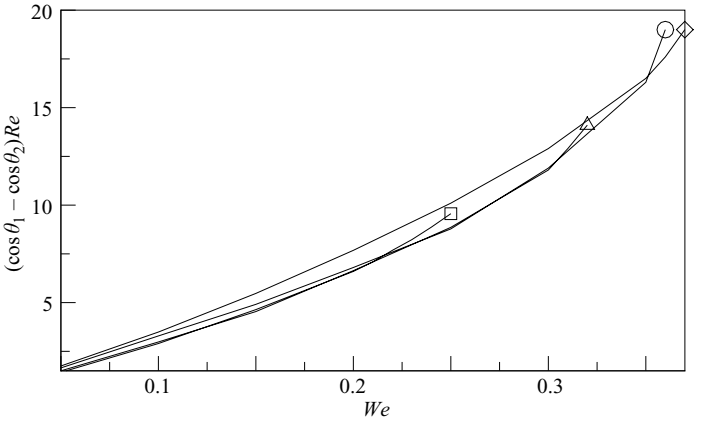

FIGURE 10. Left-hand side of (3.1) multiplied by Re as a function of We for $A = 0.5$, $\beta = 1$. □, $Re = 5$; △, $Re = 10$; ○, $Re = 15$; ◇, $Re = 25$. $N = 6$.

The orientation of the droplet is investigated in figure 8(b). In the simulations, the point was determined that is furthest removed from the halfway point between the contact lines. The angle that the line between these two points makes with the x_1-axis, denoted by θ_F, is shown in figure 8(b) versus We at various values of Re. At low Re and sufficiently low We, θ_F approaches the angle of maximum extension, 45° (Feng & Basaran 1994). At larger values of Re, θ_F remains virtually constant, at a higher value.

The circumstances under which at least one of the contact lines will start to move can be inferred from the data presented in figure 9. In figure 9, the values of the steady-state contact angles are shown as a function of We, for several Re. At low Re, the upstream (downstream) contact line can be made to move for a given value of θ_R (θ_A) by choosing We large enough for θ_1 (θ_2) to be $< \theta_R$ ($> \theta_A$). This is possible to a lesser degree at larger Re: only a narrow interval $[\theta_R, \theta_A]$ will result in a moving drop. Although the upstream contact angle is seen still to depend significantly on We at the largest value of Re for pinned drops, the downstream contact angle is virtually independent of We. If, for example, $90° - \theta_R = \theta_A - 90°$, it is normally the upstream contact line that will start to move.

Returning to the force balance (3.1), figure 10 shows the left-hand side multiplied by Re as a function of We. At low We ($\leqslant 0.12$), the results can be approximated by using $\alpha_v + \alpha_w = 26.7$, $\alpha_F = 0.33$ in (3.1). The form drag is seen to have some effect on the slope of the results in figure 10 only at the largest value of Re simulated.

The discrepancy observed in figure 4(a) between the numerical results and (3.2) can now be understood to result from the fact that, at the onset of instability at sufficiently large Reynolds number, θ_1 and θ_2 are not equal to 0°, and 180°, respectively. The fitted value for α_F in (3.1) obtained from figure 10 is different from that obtained from We_c in figure 4(a) almost by an order of magnitude. On the other hand, the fitted value for $\alpha_v + \alpha_w$ in (3.1) obtained from figure 10 is very close to that obtained from We_c in figure 4(a), confirming the finding that $We = We_c$ coincides with θ_1 and θ_2 being equal to 0° and 180° (respectively) at low Re ($\leqslant 5$).

For larger values of We in figure 10, the low-We approximation is seen to underestimate the left-hand side of (3.1). The droplet interfacial area L increases strongly, so that the drag force is expected to increase. The results are rather insensitive

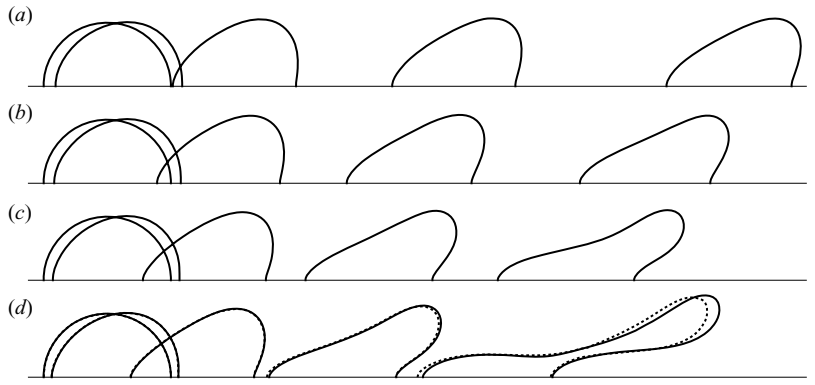

FIGURE 11. Effect of slip length λ on the stability of moving drops. Simultaneous interface shapes are shown at constant time intervals for $We > We_c$ for moving drops for $\lambda = 0.05$, 0.025, 0.0125 and 0.00625 (from top to bottom). The drops for $\lambda = 0.025$ and 0.05 are moving at constant speed and shape. The time interval between successive frames is $0.08H^2\rho/\mu$ in all cases; $\theta_A = \theta_R = 90°$; $Re = 10$, $We = 3$, $\beta = 1$, $A = 0.125$ and $N = 7$. The dashed shapes in (d) are the corresponding results when using a grid that is twice as coarse (i.e. $N = 6$).

to the value of Re; the main parameter appears to be We (for the drop size, and initial contact angles studied here).

4. Results for moving contact lines

A quasi-steady state can be achieved at We much larger than We_c reported in the previous section, by allowing the contact lines to move. Schleizer & Bonnecaze (1999) showed that, under creeping-flow conditions, Ca_c can be increased by about 50%. Our simulations show an increase in We_c that is even larger, if the sliplength is chosen sufficiently large (Schleizer & Bonnecaze (1999) fixed the value of their effective sliplength).

An example of the effect of the value of the sliplength on the flow is given in figure 11. Successive snapshots of the drop shape and location are shown for different values of λ, at $Re = 10$ and $We = 3$. It is seen that, at the largest values of λ ($= 0.025, 0.05$), the velocity of the external fluid relative to the droplet speed is low and the droplet is deformed only moderately. Figure 11(d) also shows the sensitivity to the grid spacing. Most of the results presented in this section were obtained using $N = 7$, such that the grid spacing is $1/128 = 0.00782$. The dashed lines in figure 11(d) represent the corresponding results obtained with $N = 6$, i.e. with twice the grid spacing. Only a small error in the position of the upstream contact line for the final snapshot is observed; the other shapes are almost indistinguishable.

Even although the range of λ that can be realistically simulated is very limited, fortunately, the results are sensitive to the value of λ. At $\lambda = 0.0125$, a quasi-steady state is no longer reached. At $\lambda = 0.00625$, the droplet speed is reduced by a factor of about 1.8 compared to $\lambda = 0.05$. This is seen to be sufficient for the droplet to be deformed rapidly. The deformation process is reminiscent of the low-Re behaviour shown in figure 5(a).

The Reynolds and Weber number based on the fluid velocity relative to the contact-line speed, $\gamma a - U^{cl}$ are $Re^* \equiv Re(1 - U^{cl}/(\gamma a))^2$ and $We^* \equiv We(1 - U^{cl}/(\gamma a))^3$. For $\lambda = 0.025$, these are approximately equal to 3.7 and 0.7, respectively; for $\lambda = 0.0125$, $Re^* \approx 4.9$, $We^* \approx 1$. Referring to figure 4(a), the transition to unsteady

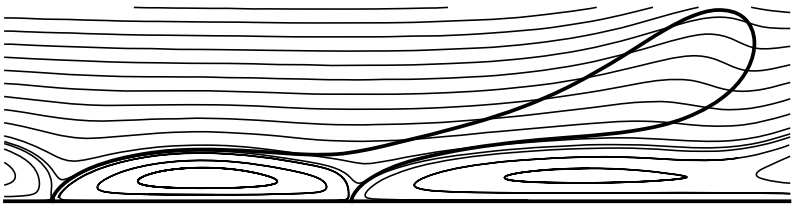

FIGURE 12. Instantaneous streamlines in a frame of reference moving with the contact lines to visualize the local velocity field, corresponding to the final snapshot of figure 11(*d*) (detail). The thick line represents the interface. The streamlines were obtained from the velocity field by using Tecplot.

flow would correspond to a point somewhat above the critical value of *We*. Therefore, although the reduction in relative fluid velocity explains most of the observed trends, $We_c(Re)$ for pinned drops can therefore only be 'translated' into a very crude approximation for We_c^* for moving drops. Other arguments for a larger value of We_c (i.e. Ca_c for creeping flows) are a possibly increased height of pinned drops, and the fixed values of the contact angles of moving droplets (Schleizer & Bonnecaze 1999).

The velocity field is illustrated for the final frame of figure 11(*d*) in figure 12. The instantaneous velocities of the two contact lines are very similar at this point, so it is helpful to subtract this velocity from the velocity field. In figure 12, instantaneous streamlines are shown corresponding to this velocity field in a frame moving with the contact lines. The instantaneous streamlines are seen to approach both contact lines from the left, approximately with a vertical tangent. The fluid departing from the left contact line inside the drop, approaches the right contact line from the left, in what appears to be a 'rolling' motion.

We now attempt to understand the transient behaviour of the speed at which the contact lines move. It is seen from figure 11 that the contact line speed is similar for both contact lines, inspection of the data shows that the upstream contact line moves only slightly faster. From figures 14(*b*) and 16(*b*) discussed further below, we can infer that the contact-line speed increases approximately linearly with $Ca = We/Re$, in agreement with Schleizer & Bonnecaze (1999). For creeping flow, Schleizer & Bonnecaze (1999) found that contact lines with contact angles of 90° also move at almost the same speed, but with the downstream contact line moving slightly faster in that case. As an aside, it should be mentioned here that Schleizer & Bonnecaze (1999) showed that this is markedly different at other contact angle values; the area wetted by drops with small (large) contact angles increases (decreases) markedly. This suggests the possibility of merging of contact lines. The wetted area is therefore shown for a droplet with 120° contact angles here in figure 13(*a*). S is defined as $X^{cl}_{(2)} - X^{cl}_{(1)}$, where $X^{cl}_{(i)}$ is the x_1—position of the ith contact line. It is seen that the contact lines approach each other until they are very close, similar to (but to a stronger degree than) the results of Schleizer & Bonnecaze (1999). Figure 13 suggests that the contact lines merge at a finite time. The contact lines appear to approach each other at almost constant speed, but the relative velocity decreases at low values of S (it is noteworthy that this occurs at values of S of the order of the slip length). The calculations have been terminated at the time when $S = 3\Delta x$, corresponding to the point of contact between the regions around each part of the interface wherein the viscosity jump is smoothed. It was found that results for later times (corresponding to even smaller values of S) are strongly grid-space dependent. Also, below a very small value of

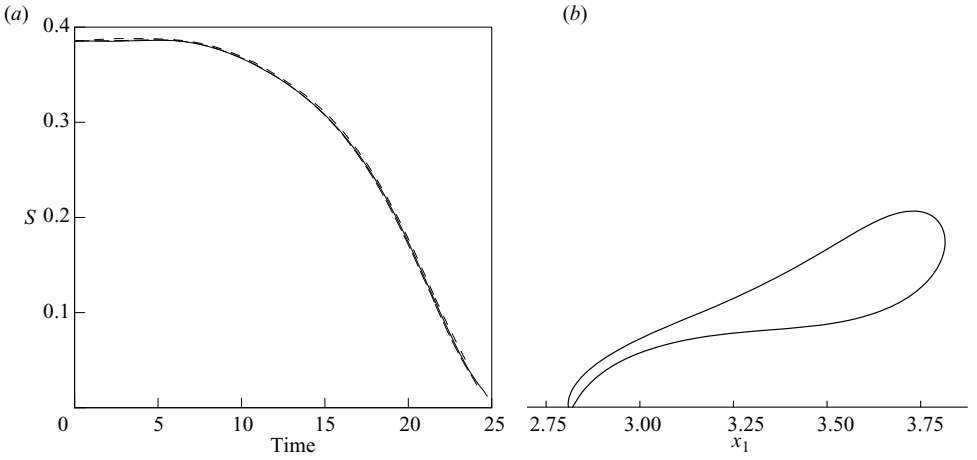

FIGURE 13. (*a*) The area S wetted by a droplet as a function of time, for contact angle 120°; $Re = 10$, $We = 3$, $A = 0.125$, $\lambda = 0.025$, $N = 6$ (short-dashed line), $N = 7$ (long-dashed line) and $N = 8$ (solid line). The upstream contact line is seen to overtake the downstream contact line. The drop shape just before the point of rupture is shown in (*b*) for $N = 8$.

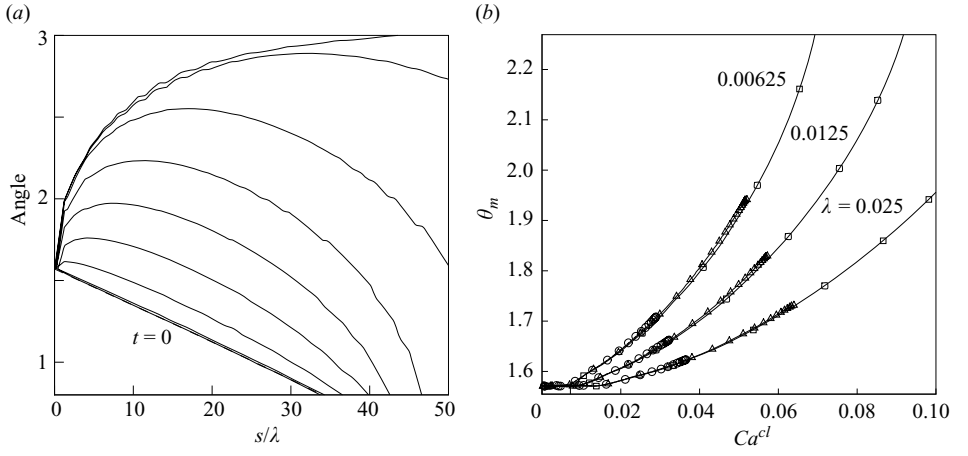

FIGURE 14. (*a*) Angle between the interface and the horizontal as a function of the distance to the downstream contact line for $Re = 10$, $We = 3$, $\beta = 1$, $\lambda = 0.00625$, $A = 0.125$, $N = 7$. The time interval between successive data is $0.04H^2\rho/\mu$. A dashed line represents the analytical result for a circular interface that coincides with the drop shape at $t = 0$, but this is not distinguishable from the numerical result for $t = 0$. (*b*) Maximum tangent θ_m as a function of Ca^{cl} of the downstream contact line for the sliplengths indicated. □, $We = 3$; Δ, $We = 1.5$; ○, $We = 0.9$. $N = 7$. The spacing between markers indicate constant time intervals. Contact angles are 90° in all cases, and $Re = 10$. The solid lines connect the data points for clarity of presentation.

S, van der Waals or other interfacial forces should be accounted for in the rupture process, but this is beyond the scope of the study.

In figure 14(*a*), the interface shape near the downstream contact line is shown at several times, for the case shown in figure 11(*d*). In figure 14(*a*), the angle that the interface makes with the horizontal is plotted versus the distance to the contact line, s. At $t = 0$, the interface is a circular cap, and this gives $\tan[\theta(s)] = s^{-1}(a - s^2/(2a))/(1 - s^2/(4a^2))^{1/2}$, which is approximately a straight line that matches the lower curve in

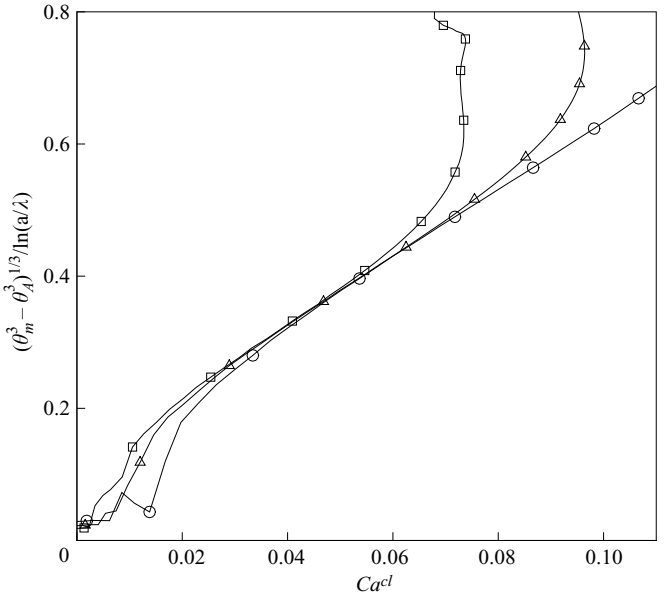

FIGURE 15. The data of figure 14(*b*) for $We = 3$, rescaled according to (4.1). □, $\lambda = 0.00625$; Δ, $\lambda = 0.0125$; ○, $\lambda = 0.025$.

figure 14(*a*) closely (plotted as a dashed line in the figure). Some wiggles in the tangent of the interface are observed. The tangent was obtained from a piecewise linear interpolation of the interface from the level-set function. The discretization errors resulting from this interpolation procedure may have some effect on the results presented here.

As time progresses, $\theta(s)$ increases rapidly at short distances from the contact line, before reaching a local maximum. This maximum angle will be denoted here by θ_m. In several studies (Tuck & Schwartz 1990; Mazouchi, Gramlich & Homsy 2004; Spelt 2005), the maximum angle is associated with the apparent contact angle in lubrication analysis for spreading droplets. The lubrication analysis of spreading of thin drops typically yields a matching condition of the form (Davis 2000)

$$\theta_d^3 = \theta_A^3 + \alpha Ca^{cl} \ln(h_0/\lambda), \tag{4.1}$$

where θ_d is the dynamic contact angle, α is a constant, and h_0 is a length scale that depends on the instantaneous drop geometry. A comparison for spreading droplets using the present method, assuming $\theta_d = \theta_m$, has been provided in Spelt (2005). We shall assume that θ_d can be set equal to θ_m; the justification for this is discussed further below. Then (4.1) would suggest that plotting θ_m versus Ca^{cl} should give an almost universal curve. 'Almost', because h_0 typically depends on the value of s beyond which $\theta \approx \theta_m$; see also Eggers & Stone (2004). This hypothesis is tested in figure 14(*b*) for the downstream contact line, by plotting θ_m against Ca^{cl} for various values of We at $Re = 10$, $A = 0.125$, for the slip length values indicated. The results for different values of We, but with the same value of λ, are seen to be very similar, as hypothesized. It should be reiterated that for the largest value of We, the droplets do not reach a steady state. Yet good agreement is observed with the drops moving at constant speed, at all times. In fact, the results appear to be governed by (4.1), with $h_0 = a$ (the initial drop radius), as can be seen in figure 15. The data in figure 14(*b*) exhibit some

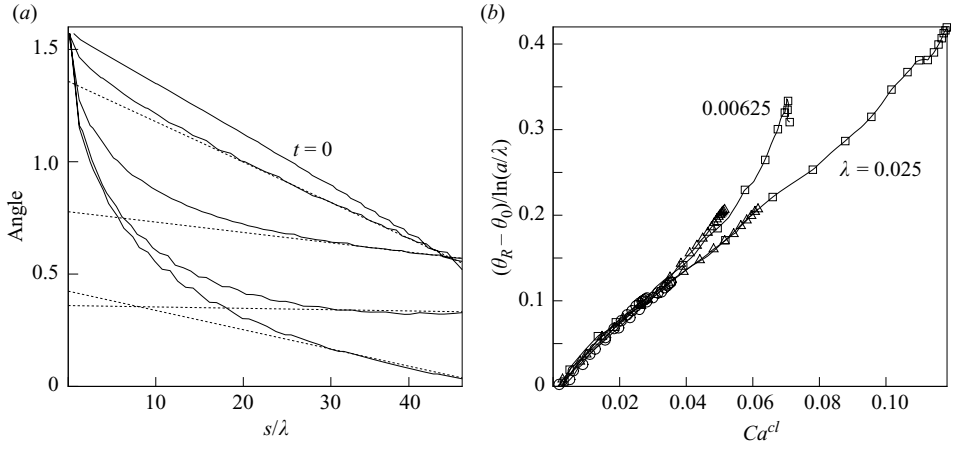

FIGURE 16. (*a*) Angle between the interface and the horizontal as a function of the distance to the upstream contact line for $Re = 10$, $We = 3$, $\beta = 1$, $\lambda = 0.00625$, $A = 0.125$, $N = 7$. The time interval between successive data is $0.08H^2\rho/\mu$. (*b*) Rescaled extrapolated angle to the wall as a function of Ca^{cl} of the downstream contact line for the sliplengths indicated. □, $We = 3$; Δ, $We = 1.5$; ○, $We = 0.9$. $N = 7$. Contact angles are 90° in all cases, and $Re = 10$. The solid lines connect the data points for clarity of presentation.

scatter during a short initial period. This is due to small errors in the determination of the maximum tangent, which are amplified when plotting the difference $(\theta_m^3 - \theta_A^3)^{1/3}$, instead of θ_m.

Despite the good agreement in figure 14(*b*), the underlying assumption of $\theta_d = \theta_m$ deserves further comment. In figure 14(*a*), $\theta(s) = \theta_m$ is seen to be satisfied only at one point, that moves away from the wall as the interface becomes more deformed. As argued by Mazouchi *et al.* (2004), this should in fact occur over a range of values of s. We will return to this issue after discussing the corresponding results for the upstream contact line.

In figure 16(*a*), the angle that the interface makes with the horizontal is plotted as a function of the distance to the upstream contact line (so s is from here onwards the distance to the upstream contact line). Starting off with the same straight line as in figure 14(*a*), the subsequent curves $\theta(s)$ merely show a stronger monotonic decrease as s is increased. Obviously, θ does not reach a maximum value near the contact line other than the imposed angle at the wall – conceptually similar to dewetting problems (Eggers 2004), in which θ varies approximately linearly far away from the contact line. As shown by Eggers (2004), not the slope but the curvature is matched between a small region around a dewetting contact line and the corresponding large-scale flow. The macroscopic contact angle in dewetting is identified as the intercept of this linear regime on the wall, which is denoted here by θ_0. Although we do not argue here that there is a one-to-one correspondence between droplet dewetting and the present problems, we do note that the results in figure 16(*a*) show a range of s ($s \geqslant 0.2$) in which $\theta(s)$ is approximately linear; the suggested extrapolation is shown as the dashed lines in the figure. In figure 16(*b*), θ_0 is plotted as a function of Ca^{cl} for various values of We at $Re = 10$, $A = 0.125$, and the sliplengths indicated. The results for a given value of λ are seen to agree very well. To summarize, the data in figures 14–16 can be represented by:

$$\theta_m^3 \approx \theta_A^3 + \left(0.12 + 5.2Ca_{(2)}^{cl}\right)\ln(a/\lambda), \quad \theta_0 \approx \theta_R - 3.5Ca_{(1)}^{cl}\ln(a/\lambda). \qquad (4.2a, b)$$

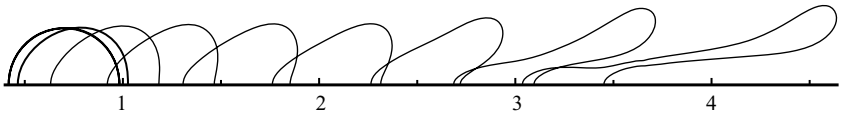

FIGURE 17. Tripping of a droplet by alteration of surface properties: the sliplength $\lambda = 0.025$ for $x_1 < 2.5$, and $\lambda = 0.00625$ elsewhere. $Re = 10$, $We = 3$, $A = 0.125$, $N = 7$. Dimensionless channel length = 6. Successive snapshots are shown at time intervals of $0.04H^2\rho/\mu$ (the first two are indistinguishable).

It should be noted that (4.2*a*) holds only for sufficiently large capillary number. Because of the extent of the required computational effort, a full parametric study has not been performed to investigate the dependence of the results shown in figures 14(*b*) and 16(*b*) on other parameters, but a test case at $Re = 25$, $We = 3$, $A = 0.125$, $\lambda = 0.0125$ was found to be very close to the corresponding results at $Re = 10$, and the results for $\lambda = 0.025$ at $A = 0.5$ virtually coincide with the results for $\lambda = 0.125$, $A = 0.125$ in figure 14(*b*) (not shown); the sliplength therefore primarily enters the relationships (4.2) through its ratio with an initial effective drop radius. We shall return to the applicability under other circumstances in the next section.

We return briefly to the results for the downstream contact line, and the use of θ_m in figure 14(*b*). The extrapolation procedure used in figure 16 for the upstream contact line suggests that a similar approach can be used for the downstream contact line. Although no particular curve fit to the data in figure 14(*a*) is obvious, we may speculate that θ_m would be an appropriate value extrapolated onto the wall from the range of s beyond the point where $\theta(s) = \theta_m$.

5. Tripping or stabilizing drops by surface property alteration

In this section, we investigate the sensitivity of the results presented above to local changes in the surface properties of the wall. In particular, we shall attempt to stabilize and destabilize moving droplets by prescribing a jump in wetting properties of the surface. In order to relate the results to those of the previous sections, the effect of changes in the slip length and the window of contact-line hysteresis are studied here seperately. The reference state used here is that of the previous section, $Re = 10$, $We = 3$, $A = 0.125$.

We first trip the droplet of figure 11(*b*) ($\lambda = 0.025$), which moves in a quasi-steady state, by changing the sliplength to $\lambda = 0.00625$ downstream, $x_1 > 2.5$. Successive snapshots are shown in figure 17. Note the reduction of drop surface area in contact with the wall, when compared to the corresponding cases with $\lambda = 0.025$ or 0.00625 throughout, shown in figure 11. After the downstream contact line has passed through $x_2 = 2.5$, the droplet area in contact with the wall is much reduced. Inspection of the results shows that fluid on the right of the upstream contact line is displaced to the upper part of the droplet, and the drop is seen to be deformed rapidly. Of course, it is no surprise that the droplet is deformed indefinitely; even if $\lambda = 0.00625$ along the entire wall, this is the case (figure 11*d*). However, the significant reduction in wetted area compared to figure 11(*d*) does provide scope for tripping drops by using a value of λ downstream for which the drop would otherwise exhibit a quasi-steady state. Because of the limitations of the computational method (it would require a large range of values of λ), such simulations are beyond the scope of the present paper.

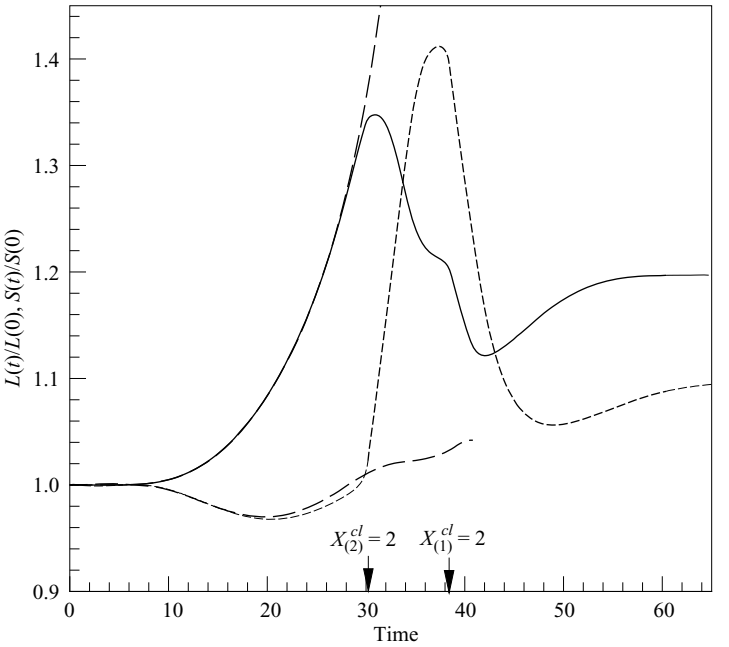

FIGURE 18. Stabilizing a droplet by alteration of surface properties: the sliplength $\lambda = 0.00625$ for $x_1 < 2$, and $\lambda = 0.025$ elsewhere. $Re = 10$, $We = 3$, $A = 0.125$, $N = 7$. Dimensionless channel length = 6. The solid and dashed line are the normalized drop surface area $L(t)/L(0)$ and the normalized wetted area, $S(t)/S(0)$. The arrows indicate when the downstream and upstream contact lines reach $x_1 = 2$. The long dashes show the corresponding results for a value $\lambda = 0.00625$ throughout (which does not reach a quasi-steady state).

Results for the reverse process are shown in figure 18. Here, the droplet of figure 11(*d*) ($\lambda = 0.00625$) is stabilized by setting $\lambda = 0.025$ at $x_1 > 2$. Once the downstream contact line has moved through $x_1 = 2$, the lower value of λ allows it to accelerate. As seen in figure 18, a strong increase results in the wetted area from this point. As a result, the drop interfacial area L decreases. Unexpectedly, once the upstream contact line has reached $x_1 = 2$, $L(t)$ continues to decrease, before increasing towards a quasi-steady state. This continuous decrease in L occurs despite the decrease in wetted area that has set in at this point.

Also shown in figure 18 are the corresponding results for $\lambda = 0.00625$ throughout. It is seen that the use of the slip condition along the entire wall does affect the contact line motion somewhat. These curves are terminated just after $t = 40$, owing to excessive deformation of the interface.

The sudden change in the local value of λ experienced by the contact lines begs the question of how well the scaling observed in figures 14(*b*) and 16(*b*) applies under these unsteady conditions. In figure 19, figure 14(*b*) is reproduced with the corresponding data for the θ_m for the tripped and stabilized drops, as a function of Ca^{cl}. In the case of the tripped drop of figure 17, θ_m is seen to depart suddenly from the result for a uniform value of $\lambda = 0.025$, just before this contact line reaches the tripping point $x_1 = 2.5$. This happens in a very short time interval. In part, this early departure can be attributed to the use of the slip condition along the entire wall, and the modest value of λ used in these simulations. Beyond this stage, θ_m has approached the result for $\lambda = 0.00625$ throughout, but not quite. For the stabilized droplet, after the

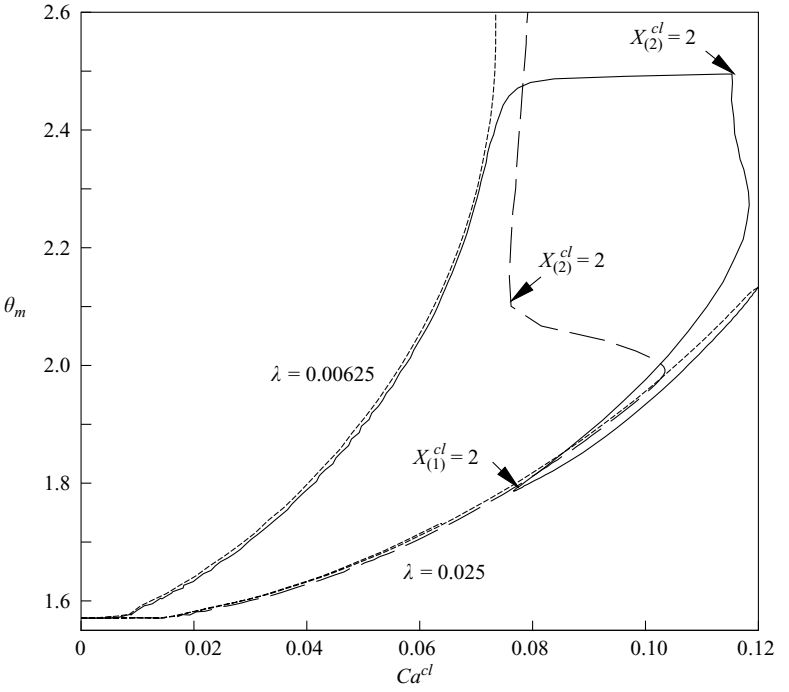

FIGURE 19. Maximum tangent as a function of Ca^{cl} of the downstream contact line for tripped (long dashes) and stabilized (solid line) drops of figures 17 and 18, respectively. The short dashes correspond to the results of figure 14(*b*).

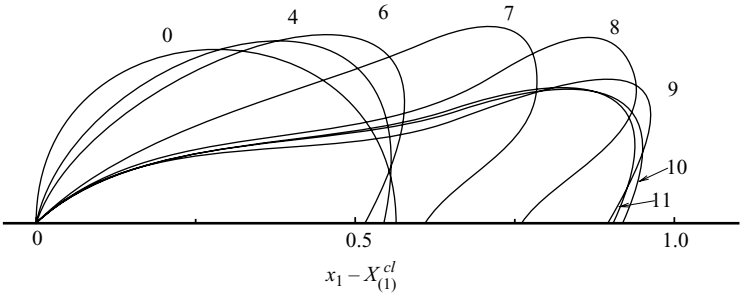

FIGURE 20. Successive snapshots of the drop shape for a droplet stabilized by alteration of surface properties, in a frame moving with the upstream contact line: $\theta_A = \theta_R = 90^\circ$ ($x_2 < 2$), $\theta_R = 60^\circ$ and $\theta_A = 100^\circ$ ($x_2 > 2$). The numbers indicate time intervals in units of $0.04H^2\rho/\mu$. $Re = 10$, $We = 3$, $A = 0.125$, $\lambda = 0.025$, $N = 7$.

downstream contact line has reached $x_1 = 2$, θ_m rapidly approaches the result for $\lambda = 0.025$ throughout (initially, Ca^{cl} decreases, until the upstream contact line has reached $x_1 = 2$, after which an increase follows). Not shown here are the results for the upstream contact line, corresponding to figures 16(*b*). A straightforward jump from the corresponding curves in figure 16(*b*) was observed when tripping or stabilizing drops.

A second way of tripping or stabilizing drops is by changing the hysteresis properties along the wall. The evolution of the drop shape is shown in figure 20. In figure 21(*a*), the interfacial area L is shown as a function of time for droplets moving on a wall

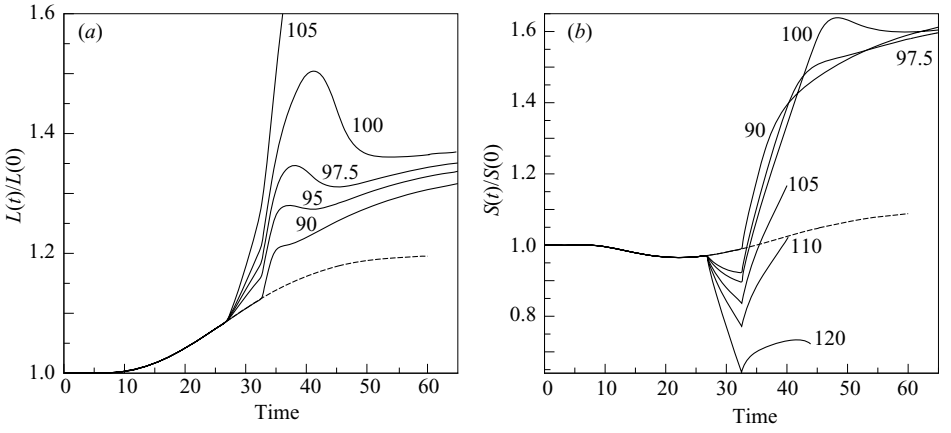

FIGURE 21. Dimensionless drop interfacial area L and wetted area S as a function of time for a wall with $\theta_A = \theta_R = 90^\circ$ ($x_2 < 2$), $\theta_R = 60^\circ$ and θ_A equal to the numbers indicated in the graph ($x_2 > 2$). The dashed lines represent $\theta_A = \theta_R = 90^\circ$ throughout. $Re = 10$, $We = 3$, $A = 0.125$, $\lambda = 0.025$.

with $\theta_R = \theta_A = 90^\circ$ for $x_1 < 2$, $\theta_R = 60^\circ$ at $x_1 > 2$ and θ_A as indicated in the figure. For comparison, the corresponding result for $\theta_R = \theta_A = 90^\circ$ for all x_1 is shown as the dashed line. The corresponding dependence of the area wetted by the droplet is shown in figure 21(*b*). At time $t = 26.81$, the downstream contact line reaches $x_1 = 2$, where it halts because of hysteresis. The wetted area decreases as the upstream contact line catches up, whereas L increases. At time $t \approx 32.6$, the upstream contact line reaches $x_1 = 2$, while the downstream contact line continues to move (hence S increases). For $\theta_A \geqslant 90^\circ$ at $x_1 > 2$, S increases to almost the same equilibrium value, or to no steady state at all (owing to rupture); a similar trend is observed for L. In particular, at $\theta_A = 120^\circ$, the wetted area is seen not to recover from the decrease caused by the wait for θ_2 to reach 120° at $x_1 = 2$. For θ_A just below the value for which the transition to rupture occurs (between 100° and 105°), $S(t)$ exhibits an overshoot before reaching the equilibrium value. It is seen in figure 20 that the initial stage of instability has just been halted in time by the change in surface properties.

6. Conclusions

Results from numerical simulations have been presented for shear flow past a two-dimensional droplet pinned or rolling on a channel wall. Because of the relatively large number of dimensionless parameters, and the large computational costs involved, we have investigated the effect of drop size (compared to the channel height), viscosity ratio, contact angle, Reynolds and Weber numbers, and dimensionless slip length for a limited number of cases. Specific issues addressed are the critical value of We beyond which no steady state can be found, and the evolution of the droplet shape in those cases. It was shown (figure 5) that, for $We > We_c$, the transient behaviour is very different at moderate values of Re, when compared to low-Re results. At moderate Re, droplets become unstable even at a moderate value of the downstream contact angle θ_2 (in the creeping-flow limit, θ_2 approaches 180° before the drop becomes unstable). An approximate value of We_c as a function of Re is generally of the form (3.2).

We_c is much increased by letting contact lines move. It was found in § 4 that, even for the limited range of slip lengths that could be simulated (λ, the smallest ratio of

slip length to channel width simulated was 0.00625), the sliplength has a significant effect on the contact-line speed. Keeping all other parameters constant, λ could be chosen such that a droplet either becomes unstable or moves at a constant speed (figure 11). Also, the simulations suggest a finite time in which two contact lines can merge in two dimensions (figure 13*a*). It is of potential benefit to know that surface properties can be chosen such that a droplet is completely sheared off from the adhering wall.

Under experimental conditions, however, the slip length is expected to be smaller than can realistically be simulated by some orders of magnitude. Nevertheless, the results presented here show that approaches in which the flow is resolved on the macroscale only may be feasible. In figures 14–16, it is seen that specific choices for macroscale contact angles scale according to (4.2) (where θ_m and θ_0 are defined as indicated in figures 14–16), i.e. independent of *We* or *Re*, for the cases simulated. The results can be represented with reasonable accuracy by the Cox–Voinov-type relations (4.2). In principle, these relations can be used in a macroscale approach, as a prescription of the contact-line speed. In Spelt (2005), such an approach was found to give converged results for spreading droplets.

The results for moving contact lines were shown in § 5 to be sensitive to local changes in the slip length or contact-angle hysteresis. It was shown that drops could be tripped or stabilized in this way. The results indicate that the relations (4.2) can be used when the sliplength varies along the wall.

The author would like to acknowledge that some of the simulations were performed at the School of Mathematical Sciences of the University of Nottingham.

Appendix. Mass conservation

The conservation of droplet size during the simulations is crucial. A loss in drop size during a simulation would stabilize the flow and require a lower surface tension for rupture of a droplet to occur. In figure 22, the total mass of a droplet is plotted as a function of time for a representative calculation, $Re = 10$, $We = 0.2$, $A = 0.125$. The dashed lines represent results in which, after each time step, the redistance step of Sussman *et al.* (1999) is used. Although sufficient mesh refinement leads to a strong decrease in mass errors, integrating the equations of motion sufficiently long will result in significant mass errors. Russo & Smereka (2000) showed that significant mass losses occur when using the redistance step algorithm of Sussman *et al.* (1994). They demonstrated that these are caused by a displacement of the interface during the redistance step, which in turn is due to the discretization of the redistance step. The interface should not move during the redistance step (which serves only to update ϕ away from the interface). Russo & Smereka (2000) proposed a fix of the redistance step discretization of Sussman *et al.* (1994). Their fix was implemented in a fluid flow solver by Spelt (2005). Following discussions on the present work at Euromech 465 and other conferences, it is desirable to supplement the previous work here with data on the conservation of mass. It is seen in figure 22 that the fix proposed by Russo & Smereka (2000) eliminates the monotonous decrease in drop size observed when using the earlier method, although small oscillations remain (their origin is discussed in Spelt (2005)).

In order to eliminate the remaining small errors, we redistribute after each time step the error in the total mass over the entire interface at the end of each time step (Sussman & Uto 1998; Spelt 2005). In figure 22, the line marked 'present' represents

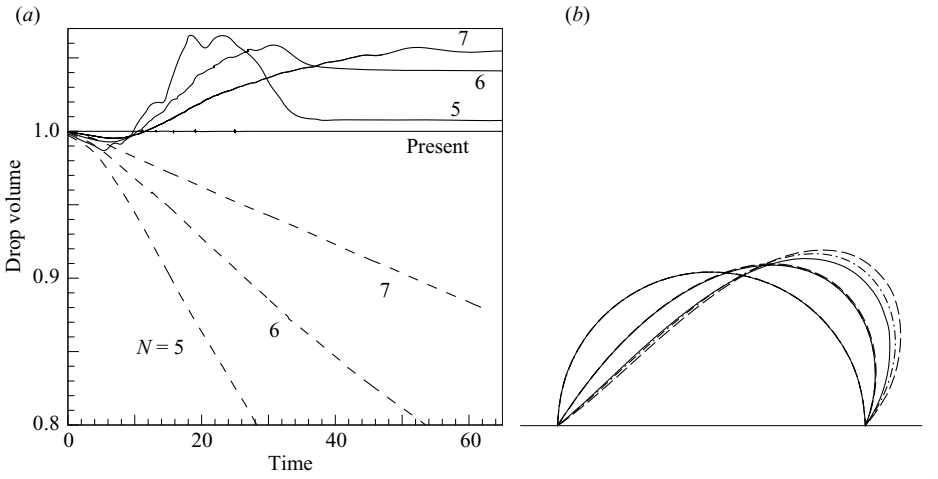

FIGURE 22. (*a*) Total drop volume normalized by the exact volume, as a function of time, for various mesh sizes. Solid and dashed lines represent results with and without the subcell fix of Russo & Smereka (2000), as implemented by Spelt (2005). The line marked 'present' represents the result with the fix, as well as with redistribution of mass errors, for $N = 6$. (*b*) Snapshots showing the effect of the redistribution of mass errors on the dynamics of the problem. The dashed and dashed-dotted lines are for $N = 6$ and 7, respectively, without using mass error redistribution. The solid lines are for the case with mass error redistribution, and $N = 6$. The time interval between successive snapshots is $0.2H^2\rho/\mu$. Pinned drop with $Re = 5$, $We = 0.5$, $A = 0.125$, $\xi = 1$, $\beta = 1$, $N = 6$.

the mass of the droplet when this final correction is used (together with the fix of Russo & Smereka 2000), at each time step just before the correction is made. It is seen that the corrections made at each time step are very small.

Although this procedure eliminates mass errors exactly, it is of some concern, as it may introduce non-physical dynamics in the results of simulations. A test case showing the effect of redistributing mass errors on the evolution of the interface is shown in figure 22(*b*). It is seen that if mass errors are not redistributed, the results appear to converge to the results obtained when mass errors are redistributed. Further evidence in support of the numerical method is presented in Spelt (2005), wherein mass errors are also redistributed throughout.

REFERENCES

BRIANT, A. J., WAGNER, A. J. & YEOMANS, J. M. 2004 Lattice Boltzmann simulations of contact line motion. I. Liquid–gas systems. *Phys. Rev.* E **69**, 031602.

BRIANT, A. J. & YEOMANS, J. M. 2004 Lattice Boltzmann simulations of contact line motion. II. Binary fluids. *Phys. Rev.* E **69**, 031603.

CAO, J., DONELL, B., DEAVER, D. R., LAWRENCE, M. B. & DONG, C. 1998 In vitro side-view imaging technique and analysis of human t-leukemic cell adhesion to ICAM-1 in shear flow. *Microvasc. Res.* **55**, 124.

CHANG, Y. C., HUO, T. Y., MERRIMAN, B. & OSHER, S. 1996 A level set formulation of Eulerian interface capturing methods for incompressible fluid flows. *J. Comput. Phys.* **124**, 449–464.

CHARCOSSET, C., LIMAYERN, I. & FESSI, H. 2004 The membrane emulsification process: a review. *J. Chem. Technol. Biotechnol.* **79**, 209.

CHATTERJEE, J. 2001 A criterion for buoyancy induced drop detachment based on an analytical approximation of the drop shape. *Colloid Surf.* A: *Physiochem. Engng Asp.* **178**, 249.

Cox, R. G. 1986 The dynamics of the spreading of liquids on a solid surface. Part 1. Viscous flow. *J. Fluid Mech.* **168**, 169.

Davis, S. H. 2000 Interfacial fluid dynamics. In *Perspectives in Fluid Dynamics* (ed. G. K. Batchelor, H. K. Moffatt & M. G. Worster), chap. 1. Cambridge University Press.

Dimitrakopoulos, P. & Higdon, J. J. L. 1997 Displacement of fluid droplets from solid surfaces in low-Reynolds-number shear flows. *J. Fluid Mech.* **336**, 351–378.

Dimitrakopoulos, P. & Higdon, J. J. L. 1998 On the displacement of three-dimensional fluid droplets from solid surfaces in low-Reynolds-number shear flows. *J. Fluid Mech.* **377**, 189–222.

Dimitrakopoulos, P. & Higdon, J. J. L. 1999 On the gravitational displacement of three-dimensional fluid droplets from inclined solid surfaces in low-Reynolds-number shear flows. *J. Fluid Mech.* **395**, 181–209.

Dimitrakopoulos, P. & Higdon, J. J. L. 2001 On the displacement of three-dimensional fluid droplets adhering to a plane wall in viscous pressure-driven flows. *J. Fluid Mech.* **435**, 327–350.

Duhar, G. & Colin, C. 2004 A predictive model for the detachment of bubbles injected in a viscous shear flow with small inertial effetcs. *Phys. Fluids* **16**, L31–L34.

Dussan V., E. B. 1979 On the spreading of liquids on solid surfaces: static and dynamic contact lines. *Annu. Rev. Fluid Mech.* **11**, 371–400.

Dussan V., E. B. 1987 On the ability of drops to stick to surfaces of solids. Part 3. The influences of the motion of the surrounding fluid on dislodging drops. *J. Fluid Mech.* **174**, 381–397.

Eggers, J. 2004 Hydrodynamic theory of forced dewetting. *Phys. Rev. Lett.* **93**, 094502.

Eggers, J. & Stone, H. A. 2004 Characteristic lengths at moving contact lines for a perfectly wetting fluid: the influence of speed on the dynamic contact angle. *J. Fluid Mech.* **505**, 309–321.

Feng, J. Q. & Basaran, O. A. 1994 Shear flow over a translationally symmetric cylindrical bubble pinned on a slot in a plane wall. *J. Fluid Mech.* **275**, 351.

de Gennes, P. G. 1985 Wetting: statics and dynamics. *Rev. Mod. Phys.* **57**, 827.

Hewitt, G. F. 1978 *Measurement of Two Phase Flow Parameters.* Academic.

Hocking, L. M. & Davis, S. H. 2002 Inertial effects in time-dependent motion of thin films *J. Fluid Mech.* **467**, 1–17.

Hodges, S. R. & Jensen, O. E. 2002 Spreading and peeling dynamics in a model of cell adhesion. *J. Fluid Mech.* **460**, 381–409.

Huh, C. & Scriven, L. E. 1971 Hydrodynamic model of steady movement of a solid/liquid/fluid contact line. *J. Colloid Interf. Sci.* **35**, 85–101.

Jacqmin, D. 2000 Contact-line dynamics of a diffuse fluid interface *J. Fluid Mech.* **402**, 57.

Jacqmin, D. 2004 Onset of wetting failure in liquid–liquid systems *J. Fluid Mech.* **517**, 209.

Leal, L. G. 1992 *Laminar Flow and Convective Transport Processes.* Butterworth–Heinemann.

Li, X. & Pozrikidis, C. 1996 Shear flow over a liquid drop adhering to a solid surface. *J. Fluid Mech.* **307**, 167–190.

Magnaudet, J., Bonometti, T. & Benkenida, A. 2006 The modelling of viscous stresses for computing incompressible two-phase flows on fixed grids. Preprint.

Mazouchi, A., Gramlich, C. M. & Homsy, G. M. 2004 Time-dependent free surface Stokes flow with a moving contact line. I. Flow over plane surfaces. *Phys. Fluids* **16**, 1647–1659.

Minnaert, M. 1974 *De Natuurkunde van't Vrije Veld: Rust en Beweging.* (in Dutch). Thieme.

Russo, G. & Smereka, P. 2000 A remark on computing distance functions. *J. Comput. Phys.* **163**, 51–67.

Schleizer, A. D. & Bonnecaze, R. T. 1999 Displacement of a two-dimensional immiscible droplet adhering to a wall in shear and pressure-driven flows. *J. Fluid Mech.* **383**, 29–54.

Shikhmurzaev, Y. D. 1997 Moving contact lines in liquid/liquid/solid systems. *J. Fluid Mech.* **334**, 211.

Spelt, P. D. M. 2005 A level-set approach for simulations of flows with multiple moving contact lines with hysteresis. *J. Comput. Phys.* **207**, 389–404.

Sussman, M. & Uto, S. 1998 A computational study of the spreading of oil underneath a sheet of ice. *CAM Rep.* 98–32.

Sussman, M., Smereka, P. & Osher, S. 1994 A level set approach for computing solutions to incompressible two-phase flow. *J. Comput. Phys.* **114**, 146–159.

Sussman, M., Almgren, A. S., Bell, J. B., Colella, P., Howell, L. H. & Welcome, M. L. 1999 An adaptive level set approach for incompressible two-phase flows. *J. Comput. Phys.* **148**, 81–124.

Tuck, E. O. & Schwartz, L. W. 1990 A numerical and asymptotic study of some third-order ordinary differential equations relevant to draining and coating flows. *SIAM Rev.* **32**, 453–460.

Wakiya, S. 1975 Application of bipolar coordinates to the two-dimensional creeping motion of a liquid. I. Flow over a projection or a depression on a wall. *J. Phys. Soc. Japan* **39**, 1113–1120.

Yon, S. & Pozrikidis, C. 1999 Deformation of a liquid drop adhering to a plane wall: significance of the drop viscosity and the effect of an insoluble surfactant. *Phys. Fluids* **11**, 1297–1308.